JOURNAL OF PROPULSION AND POWER
Vol. 19, No. 3, May–June 2003

Normal Shock/Boundary-Layer Interaction Control Using Aeroelastic Mesoflaps

Everett S. Hafenrichter,* Yeol Lee,† J. Craig Dutton,‡ and Eric Loth§
University of Illinois at Urbana–Champaign, Urbana, Illinois 61801

A normal shock/boundary-layer interaction control technique termed mesoflaps for aeroelastic recirculating transpiration has been investigated in a planar Mach 1.37 wind tunnel. In this flow-control system, an array of small flaps is mounted over a cavity; the flaps deflect aeroelastically under the pressure loads imposed by the normal shock, thereby allowing recirculation from downstream of the shock to upstream. Qualitative analysis of the mesoflap control was investigated with spark shadowgraph visualizations and oil-streak surface-flow visualizations, whereas quantitative analysis was achieved by measuring surface pressure distributions and boundary-layer velocity profiles. Nine different mesoflap arrays were investigated, in addition to the solid-wall reference case. It was found that flap thickness and, therefore, transpiration rate, had a demonstrable effect on static and total pressure recovery, in addition to boundary-layer integral properties. Although some of the arrays did not provide a performance benefit, one particular flap array was found to have significantly higher static and total pressure recoveries than the solid-wall reference case, while simultaneously demonstrating a reduction in boundary-layer momentum thickness and unchanged displacement thickness.

Introduction

Background

THE interaction of a shock wave with a boundary layer can have a major impact on the inlet efficiency of supersonic vehicles. The adverse pressure gradient associated with the shock system typically leads to poor boundary-layer characteristics and can often cause separation. In addition, shock/boundary-layer interactions (SBLIs) play an instrumental role in determining the total pressure recovery associated with any supersonic inlet design. Thus, successfully controlling SBLIs has the potential to improve supersonic inlet performance significantly.

One proven method for controlling SBLIs is to "bleed off" the low-momentum portion of the boundary layer, thereby avoiding boundary-layer separation and improving overall flow uniformity. Boundary-layer bleed is currently employed in several supersonic aircraft, most with cruising speeds above Mach 2 (Ref. 1). Although bleed effectively controls the SBLI, there are several disadvantages. Bleeding can significantly increase inlet capture area and, therefore, weight and drag because more mass flow is needed to compensate for the low-momentum flow dumped overboard. In addition, bleed requires ducting, which occupies valuable space and increases the overall weight and cost of the vehicle.

One alternative to boundary-layer bleed is recirculating control, which is often called "passive control."[2–9] This control method takes advantage of the pressure rise across the shock system by placing a cavity covered by a porous medium under the shock foot. This porous medium typically consists of a plate machined with normal and/or angled holes or slots. The pressure rise across the shock is communicated through this porous medium to the cavity, resulting in a natural recirculation of the air from the high-pressure downstream side of the shock to the low-pressure upstream side. Previous studies[5,6] have shown that recirculating control can have a positive impact on total pressure recovery, thereby improving wave drag. Unfortunately, these studies have also shown that conventional recirculating control detrimentally affects the boundary-layer displacement and momentum thicknesses, resulting in an increase in viscous drag.

The present study takes a different approach to recirculating control than previous work. Instead of a machined plate, an array of small flaps, termed mesoflaps for aeroelastic recirculating transpiration (MART), is placed beneath the normal shock foot (Fig. 1a). These flaps are fixed at their upstream end to a spar, whereas the majority of the flap can aeroelastically deflect according to the pressure loads imposed by the shock system, resulting in a recirculation of the flow similar to conventional passive control. The flaps downstream of the shock foot deflect downward, according to the pressure increase across the shock. This allows for removal of the low-momentum portion of the boundary layer in a fashion similar to conventional boundary-layer bleed. Upstream of the main normal shock, however, the flaps deflect upward into the low-pressure region preceding the shock system. The flow bled off through the downstream flaps is reinjected through the upstream flaps, thus potentially energizing the low-momentum portion of the upstream boundary layer and allowing oblique-shock precompression due to the upward flap deflections. Because the deflections are kept relatively small, the MART system possesses an aerodynamic advantage over conventional normal or angled recirculating control by allowing for nearly tangential bleed downstream and nearly tangential blowing upstream. Furthermore, the flaps revert to a nearly smooth solid wall for subsonic conditions (Fig. 1b), thereby minimizing the roughness and increase in friction drag associated with conventional passive control techniques at off-design conditions.

Previous work[10–13] at the University of Illinois at Urbana–Champaign has used experimental and computational methods to study the performance of mesoflap arrays in the context of an oblique-shock interaction ($M = 2.45$). The present work expands on this by experimentally studying the potential of the mesoflaps to control normal shock wave/boundary-layer interactions ($M = 1.37$). Spark shadowgraph visualizations, surface oil-flow visualizations, surface static pressure distributions, and measurements of boundary-layer mean velocity profiles are presented.

Received 18 June 2002; revision received 6 January 2003; accepted for publication 13 January 2003.

*Graduate Research Assistant, Department of Mechanical and Industrial Engineering. Member AIAA.

†Visiting Associate Professor, Department of Mechanical and Industrial Engineering; currently Associate Professor, School of Aerospace and Mechanical Engineering, Hankuk Aviation University, 200-1 Hwajon-Dong, Koyang-Si, Kyunggi-Do, 412-791, Republic of Korea. Senior Member AIAA.

‡W. Grafton and Lillian B. Wilkins Professor, Department of Mechanical and Industrial Engineering. Associate Fellow AIAA.

§Professor and Willett Faculty Scholar, Department of Aeronautical and Astronautical Engineering. Associate Fellow AIAA.

Description of Facility

All experiments were conducted in the Gas Dynamics Laboratory at the University of Illinois at Urbana–Champaign. The blowdown normal shock facility (Fig. 2) is supplied with desiccated high-pressure air and exhausts to the atmosphere. A description of the test section in its original configuration can be found in Ref. 14. Gefroh modified the facility for Mach 2.45 oblique-shock studies of mesoflap arrays, as described in Ref. 13. For the present investigation, a new converging–diverging nozzle block was manufactured using the method of characteristics design code of Carroll et al.[15] This nozzle block provides uniform Mach 1.37 flow, with a unit Reynolds number of 30×10^6 m^{-1} in the 50.8×50.8 mm test section. A more detailed description of the facility in its normal shock configuration can be found in Ref. 16.

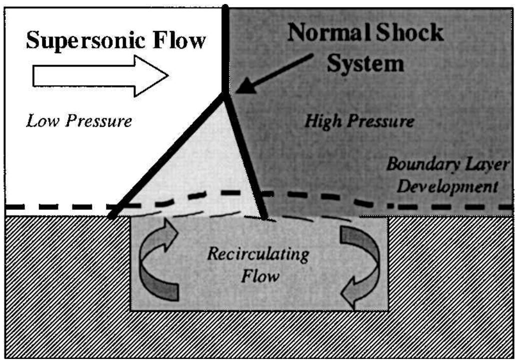

a) MART array in supersonic flow

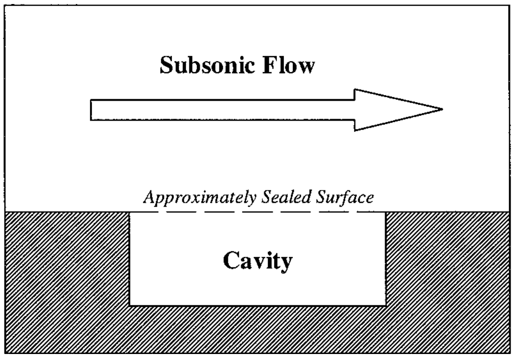

b) MART array in subsonic flow

Fig. 1 Schematic of the MART concept.

The cavity in this investigation was located slightly downstream of the exit of the nozzle contour, with the leading edge starting 10.03 mm downstream of the contour end. The cavity spanned the entire 50.8 mm width of the test section and was 44.45 mm long and 19.05 mm deep.

The position of the normal shock was controlled directly by varying tunnel stagnation pressure using a Fisher TL101 process controller. The back pressure remained constant at a level slightly higher than atmospheric pressure, due to losses in the exhaust ductwork. The tunnel stagnation pressure varied slightly depending on test conditions and the particular MART array being studied, but was usually around 210 kPa. Stagnation temperature remained approximately constant throughout the experiments at 300 K.

Flap Array Descriptions

Figure 3 shows a schematic of the flap arrays studied in the present work. Figure 3a depicts a third-generation six-flap array, whereas Fig. 3b depicts a four-flap variant of the third-generation design. The first- and second-generation designs and their subsequent evolution to the third-generation design are discussed by Gefroh et al.[10] and Gefroh.[13] The four-flap design allowed for the examination of thicker, and, thus, more mechanically robust, flaps, while still achieving sufficient deflections due to the increased length of the flaps. In addition, preliminary computational fluid dynamics (CFD) results indicated that four-flap arrays would perform better than their six-flap counterparts. Each flap array, manufactured from a nickel–titanium alloy termed Nitinol, measures 57.15 mm in length and 50.8 mm in width. The flaps are mounted on a stainless steel stringer plate, which supports the flaps in all static areas. The six-flap stringer measures 1.19 mm in thickness, whereas the four-flap stringer is 0.79 mm thick. The leading edges of the spanwise-running spars of the stringer are machined to a sharp angle for aerodynamic purposes (Fig. 3). Each stringer is mounted to an aluminum frame, which fastens over the test-section cavity via four hex-headed bolts. Rubber gaskets of differing thicknesses are used to assure a tight seal and flush fit between the frame and cavity.

Several flap thicknesses were studied to achieve different levels of flap deflections, thereby investigating the effect of flap deflection on flow recirculation, and, ultimately, the efficiency of the flaps in controlling the SBLI. Five different six-flap mesoflap arrays were examined, with thicknesses of 63.5, 78.2, 101.9, 127.5, and 150.6 μm. In addition, four different four-flap mesoflap arrays were studied, with thicknesses of 127.5, 150.6, 190.5, and 228.6 μm.

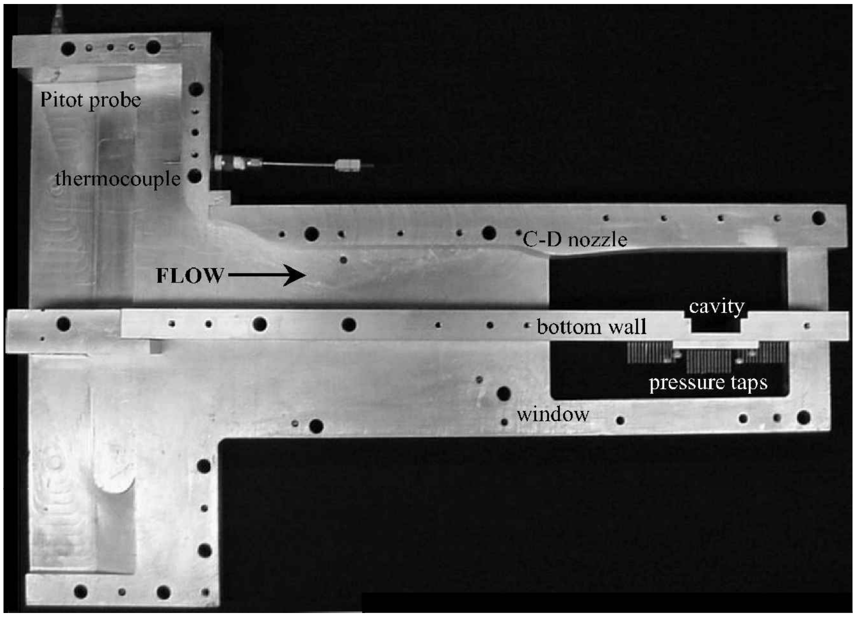

Fig. 2 Photograph of test section with sidewall removed.

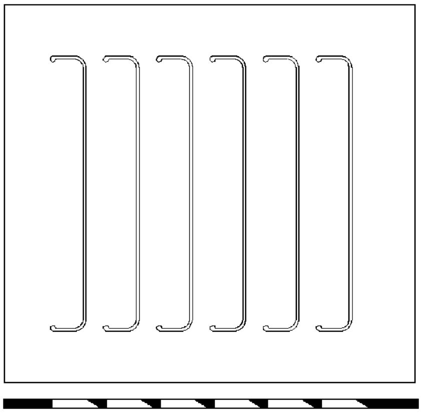

a) Six-flap MART array

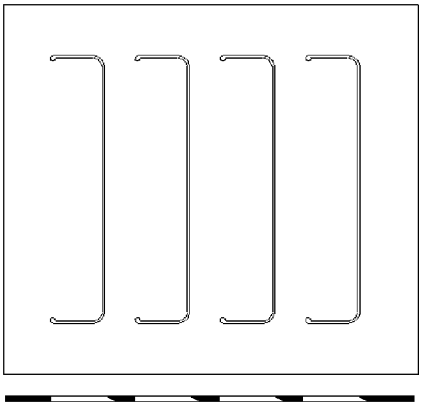

b) Four-flap MART array

Fig. 3 Top view of MART arrays, with stringer profiles shown below.

Results

Flap Deflection Observations

Before the experimental results are presented in detail, some general observations about flap behavior are discussed. In the case of the extremely thin flaps, primarily the 63.5-μm six-flap array and 127.5-μm four-flap array, flap deflections were occasionally large, that is, greater than 2 mm. Generally, these large deflections were accompanied by fluttering of the flaps, which then often led to mechanical failure of the MART array within minutes of testing. The failure was attributed to cracks propagating from the stress-relieving holes located at the leading edge of the flaps (Fig. 3). These cracks would then propagate until a corner of the flap was torn off, or until the entire flap array was sheared from the steel stringer. As a result of limited testing time because of array failure, a reduced amount of laser Doppler velocimetry (LDV) data were gathered for these two cases. Slight fluttering was observed with the other MART arrays investigated, with the exception of the 127.5- and 150.6-μm six-flap arrays and the 228.6-μm four-flap array, which remained motionless with an extremely small amount of flap deflection.

Shadowgraph Visualizations

Spark shadowgraphs were captured on Polaroid Type 55 land film using a Xenon Model 457 Micropulser as the light source (1.4-μs spark duration). Shadowgraphs of the SBLI were obtained for the solid-wall reference case, in addition to eight of the mesoflap arrays. In the interest of space, a limited number of representative shadowgraphs will be presented and discussed here. Additional details are given in Ref. 16.

Figure 4a shows the normal shock interaction with the solid wall (flow is from left to right). Note that the lower black surface in the shadowgraph is the lower wall of the test section, whereas the upper wall is actually located 12.7 mm above the top edge of the window. The interaction seen in Fig. 4a is consistent with a classical normal SBLI: The boundary layer thickens sharply at the shock foot, resulting in a relatively short leading oblique shock. This gives rise to the familiar "lambda" shape of the SBLI. The small triangular region of still supersonic flow downstream of the leading oblique shock is terminated by a nearly normal trailing shock. The boundary layer downstream of the interaction is clearly significantly thicker than the incoming boundary layer. Analysis of the LDV mean velocity profiles indicates an incoming boundary-layer thickness of 2.6 mm, with an outgoing boundary-layer thickness of 7.0 mm, an increase of almost threefold.

The Mach wave that intersects the normal shock near its center is a result of the small redirection of flow at the end of the C–D nozzle contour. This wave, which is certainly weak, is visible in all of the shadowgraphs discussed and is expected to have a negligible influence on the SBLI. Also, weak normal waves can be detected in the flow downstream of the normal shock in Fig. 4a. These disturbances are typical of transonic flow patterns.

Figure 4b displays the interaction of the normal shock with the six-flap 63.5-μm thickness MART array. The shock structure developed in this interaction is in clear contrast to the solid-wall SBLI depicted in Fig. 4a. The short leading oblique shock seen in Fig. 4a is replaced with a series of three longer leading oblique shocks, resulting in a much larger lambda shape. The first of these leading shocks is a weak wave that originates from the junction of the flap array with the tunnel wall. A close inspection of the shadowgraph reveals that the first three flaps protrude into the incoming supersonic flow; the locations of these three upstream flaps define the position of the array sketched in Fig. 3a over the cavity. The "ramp" created by the upward deflection of the first flap is the origin of the second oblique shock. The third shock seems to be caused by the injection of flow from the first flap and/or by the upward deflection of the second flap.

A weak secondary normal shock can be observed downstream of the interaction near the trailing edge of the cavity in Fig. 4b. One hypothesis for the existence of this shock is as follows: During the initial portion of the interaction, the boundary layer can be seen to thicken due to the adverse pressure gradient and flow injection from the upstream flaps. As the downstream flaps bleed off the low-momentum portion of the boundary layer, the boundary layer begins to thin. The freestream flow sees the increase and subsequent decrease of the boundary-layer thickness as an aerodynamically formed converging–diverging nozzle and reaccelerates to supersonic conditions. This phenomenon, which is closely related to the behavior of classical shock trains,[17] gives rise to the secondary recompression normal shock, which can be seen in all of the MART shadowgraphs presented. The secondary shock suggests that the downstream flaps effectively bleed off the boundary layer because the resulting decrease in boundary-layer thickness is sufficient to give rise to the secondary shock, which is not seen in the solid-wall shadowgraph. Because this secondary shock appears to be quite weak in the shadowgraphs, it most likely does not affect the total pressure recovery substantially.

Figures 4c and 4d present shadowgraphs of six-flap arrays with thicknesses of 101.9 and 150.6 μm, respectively. Although the line-of-sight integrating nature of the shadowgraph method must be considered, the shock systems show slight differences when compared to the thinner flap array of Fig. 4b. The first two leading oblique shocks in Fig. 4c look similar to their counterparts in Fig. 4b, but the third shock (due to injection from the first flap) shows subtle differences. Indeed, there seem to be two separate shocks originating from this single location. The first of these shocks looks strikingly similar to a bow shock, whereas the second shock looks similar to an oblique shock originating from a wedge. This suggests that the upstream injection for these thicker arrays has become more transverse, resulting in a bow shock typical of transverse jets in supersonic flow.[18] The second shock of this pair is likely the result of the deflection of the second flap up into the supersonic freestream flow. This same shock pattern is even more evident in Fig. 4d, where the flaps are 150.6-μm thick. In this case, there seem to be two such two-shock structures, originating downstream of both the first and second flaps. This indicates that the thicker flap arrays inject flow

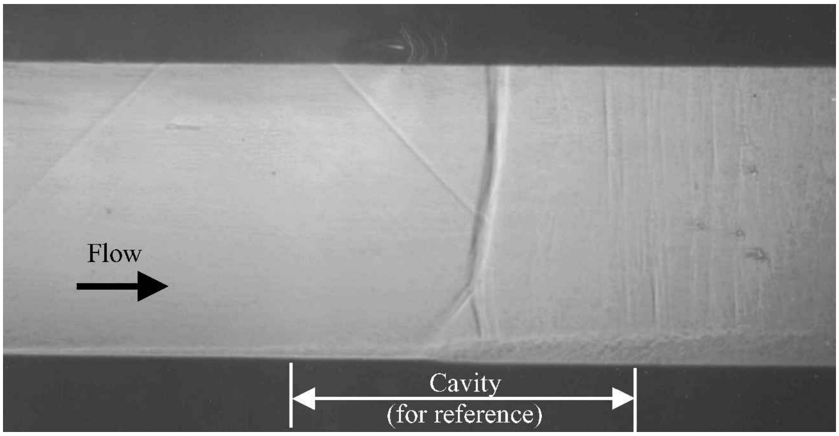

a) Solid-wall reference case

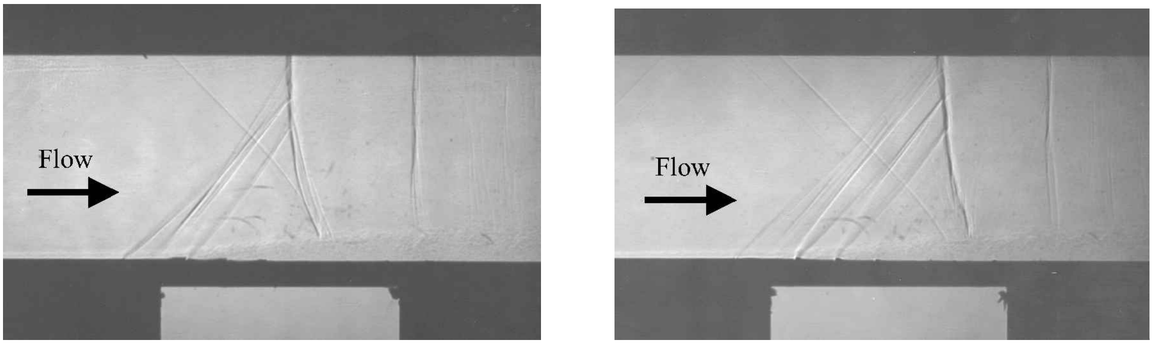

b) Six-flap 63.5-μm MART array

d) Six-flap 150.6-μm MART array

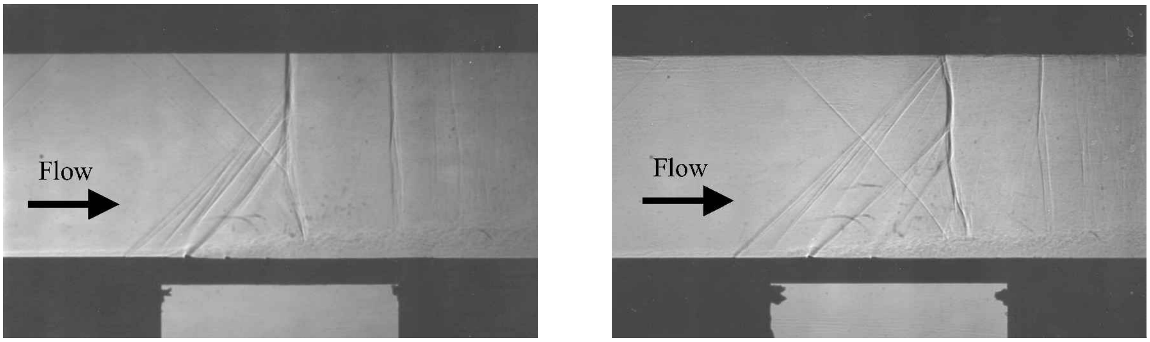

c) Six-flap 101.9-μm MART array

e) Four-flap 190.5-μm MART array

Fig. 4 Shadowgraph visualizations.

transversely, instead of tangentially, as expected, because flap deflections are extremely small for these cases. Note that the flaps can not be seen deflecting upward into the flow with the thicker arrays of Figs. 4c and 4d. Also, note that transverse injection is likely to be more detrimental to the resulting boundary-layer characteristics than is tangential injection.

Figure 4e presents a shadowgraph of the four-flap 190.5-μm array. The shock structure is similar to the earlier shadowgraphs of the MART arrays, with weak bow shocks present at the two upstream injection sites. These injection locations define the position of the four-flap array (Fig. 3b) over the cavity. The normal shock has a tendency to sit further downstream of the center of the cavity with the four-flap 190.5-μm flap array, in a similar fashion to the six-flap 150.6-μm flap array (Fig. 4d). Shadowgraphs of the other four-flap arrays[16] indicated that the thinner and thicker arrays yielded shadowgraphs that reinforced the trends observed with the six-flap arrays (discussed earlier).

These shadowgraphs for the mesoflap arrays suggest a probable increase in stagnation pressure recovery (or a decrease in wave drag) with respect to the solid wall, due to the "shock smearing" effect of the lambda-shock system, sometimes called the "lambda-shock benefit."[6] The injection of flow upstream of the normal shock weakens the single normal shock strength by causing leading oblique shocks. The irreversibility induced by the multiple-shock system is, therefore, reduced compared to the single shock of the reference case. This benefit is well documented in the literature,[2–9] but is usually associated with an increase in viscous drag, primarily due to increased boundary-layer momentum thickness.[6] Quantitative results for the integral boundary-layer thicknesses will be presented in a later section.

Surface-Flow Visualizations

A mixture of carbon black, STP oil treatment, and kerosene was used to create oil-streak surface-flow visualizations on the bottom wall and one of the window sidewalls. These samples were captured on transparent tape and are depicted in Fig. 5.

The solid-wall surface-flow visualization (Fig. 5a) indicates that a region of separation exists just downstream of the normal shock interaction, due to the pooling of oil that occurs in this region. The pattern on the sidewall also suggests separation, with a region of roll-up clearly evident in the oil pattern. The increase in boundary-layer thickness across the interaction is also clearly evident in the

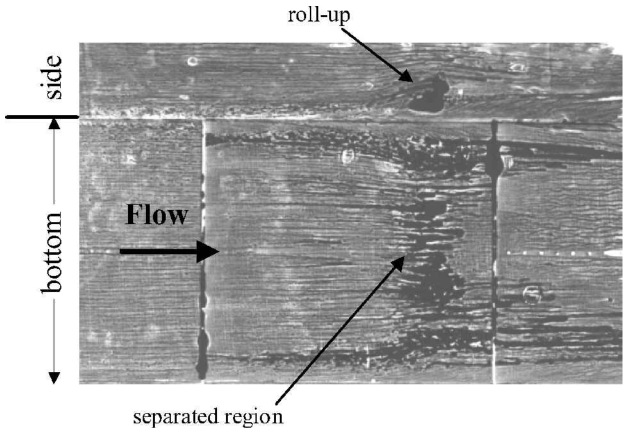

a) Solid wall

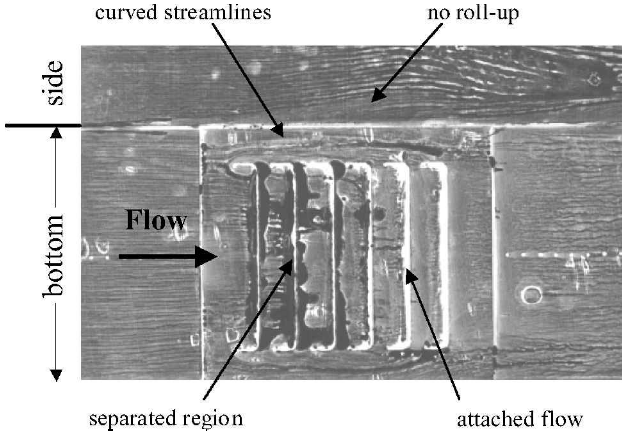

b) MART array (six-flap 101.9 μm)

Fig. 5 Surface-flow visualizations.

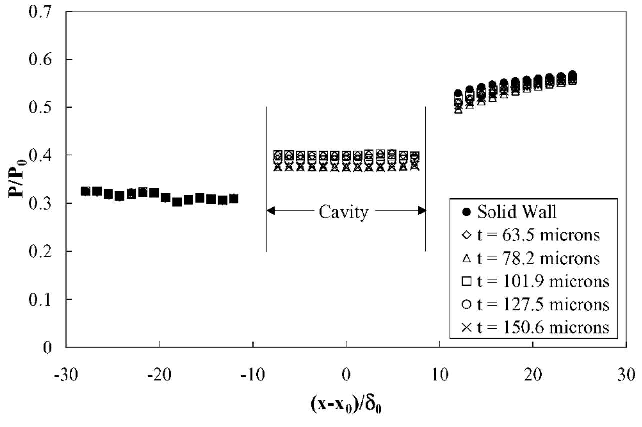

a) Six-flap MART arrays

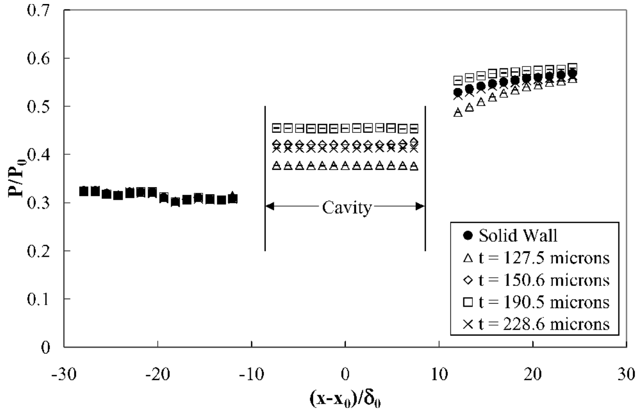

b) Four-flap MART arrays

Fig. 6 Centerline static pressure distributions (note that the uncertainty bars are smaller than the data symbols).

surface-flow pattern on the window sidewall. The small white-ringed blotches on the oil-flow patterns are the result of small air pockets trapped between the transparent tape and oil-streak pattern and should be ignored.

The surface-flow visualization with a mesoflap array in place (Fig. 5b) reveals several interesting characteristics of the flow. The streaklines along the sides of the first few flaps are slightly curved away from the streamwise-running slots, indicating a transverse jet effect from the cavity into the freestream in these regions. This is consistent with the bow shocks observed in the shadowgraph for this case (Fig. 4c). In the side regions of the downstream flaps, the streaklines are curved toward the side slots, indicating flow ingestion into the cavity in these regions. The oil patterns over the upstream flaps suggest separation, although this separation is not as evident in the sidewall oil pattern compared to the solid wall. The oil patterns over the downstream flaps indicate that the flow is reattached, suggesting that the flaps effectively bleed off the boundary layer, which is again consistent with the shadowgraph visualizations. Overall, the surface-flow patterns for the solid-wall and mesoflap arrays suggest a relatively two-dimensional flow, except in the neighborhood of the streamwise slots, as discussed earlier.

Surface Pressure Distributions

Pressure taps located along the test-section spanwise centerline recorded surface static pressure at 38 streamwise locations (spacing of 3.18 mm), including 14 taps upstream of the cavity, 13 taps along the cavity bottom, and 11 taps downstream of the cavity. Static pressure data were not acquired in the cavity region for the solid wall because a blank plate with no pressure taps was mounted over the cavity in this case. All data presented here represent the average of 50 individual pressure measurements. Measurements were acquired with a Pressure Systems, Inc. digital pressure transmitter (model DPT 98RK), which possesses a measurement accuracy of ±0.05% of the full-scale reading.

Figure 6a shows the static pressure distribution for the six-flap MART arrays, as well as the solid-wall reference case. Streamwise location, $x^* = (x - x_0)/\delta_0$, is nondimensionalized by the incoming boundary-layer thickness ($\delta_0 = 2.6$ mm) and is defined to be zero at the cavity center x_0. Static pressure is nondimensionalized by the tunnel stagnation pressure P_0. As expected, the incoming static pressure distribution is nearly constant and is identical for all cases. The static-to-stagnation pressure ratio P/P_0 is indicative of a Mach 1.37 incoming flow. The static pressure rises across the shock interaction by a factor of 1.9 (compared to a factor of 2.0 predicted by one-dimensional normal shock wave theory for Mach 1.37 flow), and a static pressure between the high-pressure downstream side and low-pressure upstream side is achieved along the bottom of the cavity. This medium cavity pressure indicates that the flaps perform as predicted, with flow recirculating through the cavity. The pressure in the cavity is similar for all flap arrays studied, with small variations in magnitude. The 78.2- and 150.6-μm flaps have the lowest cavity pressure, whereas the 63.5- and 101.9-μm flaps have the highest cavity pressure. The 127.5-μm flap array possesses a cavity pressure between these two other pairs. In all cases, pressure is essentially constant throughout the cavity length, as found in previous studies.[6,10,12] Although a trend linking cavity pressure to flap thickness is difficult to decipher, one trend is easily observed: The cases with higher cavity pressure also have higher downstream wall-static pressures. For all six-flap arrays, however, the downstream static pressure is slightly lower than the solid-wall reference case, with the 101.9-μm array achieving the highest downstream pressure.

Figure 6b depicts the static pressure distributions of the four-flap MART arrays, again with the solid wall shown as a reference. Although these results appear similar to the six-flap results, there are some important differences. The cavity pressure varies greatly between the four-flap arrays, in contrast to the findings of Bur et al.[6] for conventional porous plates and the modest variations found by Gefroh et al.[10,12] for oblique-shock/MART interactions (six-flap cases). Furthermore, the results indicate that cavity pressure is maximum for the 190.5-μm array. Downstream, the same trend observed with the six-flap MART pressure distributions dominates: Higher cavity pressure is accompanied by higher downstream pressure. The downstream pressures of the 150.6- and 228.6-μm MART arrays are almost identical to the solid-wall reference case, whereas the downstream pressure of the 190.5-μm MART array is significantly higher than the reference case. It will be shown in the next section that an increase in downstream static pressure is a preliminary indication of an increase in total pressure recovery, a result that is consistent with the oblique-shock case of Gefroh et al.[10,12]

Boundary-Layer Velocity Measurements

A TSI fiber-optic LDV system was used to acquire centerline mean velocity profiles at several streamwise locations. The system utilized the 514.5-nm line from a 5-W argon–ion laser, and was operated in forward-scatter mode for maximum signal-to-noise ratio. One-component LDV measurements of the streamwise velocity component were utilized to achieve maximum spatial resolution near the wall (first measurement at $y = 0.20$ mm above the wall). The measurement probe volume (diameter of 119 μm) was traversed through the flowfield using a computer-controlled traversing system with spatial resolution better than 5 μm. The flow was seeded with submicron silicone oil droplets,[19] and all data were velocity debiased by the particle interarrival time method, as suggested by Herrin and Dutton.[20] The mean velocity at each measurement point in the flowfield was determined from 4000 instantaneous realizations, and the overall maximum uncertainty in streamwise velocity was 2.1% of U_0 (Ref. 16). A more complete description of the LDV system and the measurement method can be found in Refs. 10, 13, and 16.

The incoming velocity profile at $x^* = -17.3$ (17.3 boundary-layer thicknesses upstream of the cavity center) is shown in Fig. 7. Although these data were obtained with the solid wall in place, the incoming profile at this streamwise location is identical with MART arrays mounted over the cavity. The velocity profile is characteristic of a fully developed, turbulent boundary layer, with a freestream velocity U_0 of 405 m/s and a boundary-layer thickness (99%) δ_0 of 2.6 mm. Numerically integrating the profile to obtain the incompressible displacement and momentum thicknesses yields values of $\delta_0^* = 0.356$ mm and $\theta_0 = 0.203$ mm. These values will be used to nondimensionalize all subsequent plots.

Outgoing velocity profiles were obtained at four separate streamwise stations downstream of the SBLI. These stations were located 12.0, 15.7, 19.3, and 23.0 boundary-layer thicknesses downstream of the cavity center. Although a few representative outgoing velocity profiles will be discussed here (with the remainder given in Ref. 16), the boundary-layer integral parameters for all of the cases examined will subsequently be presented.

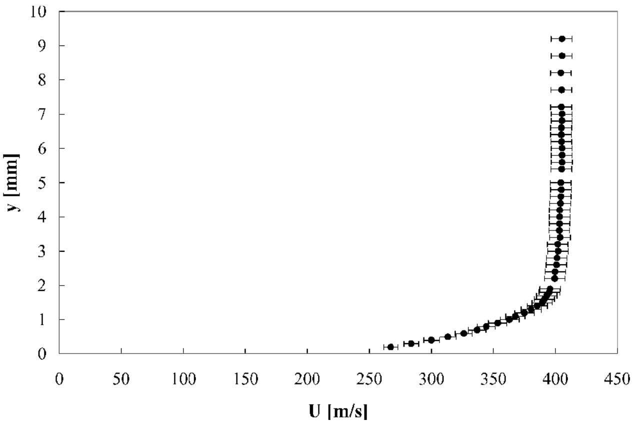

Fig. 7 Incoming velocity profile ($x^* = -17.3$).

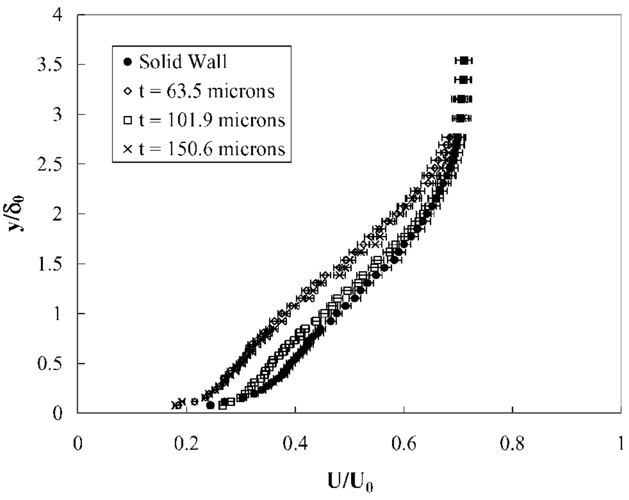

a) Six-flap MART arrays

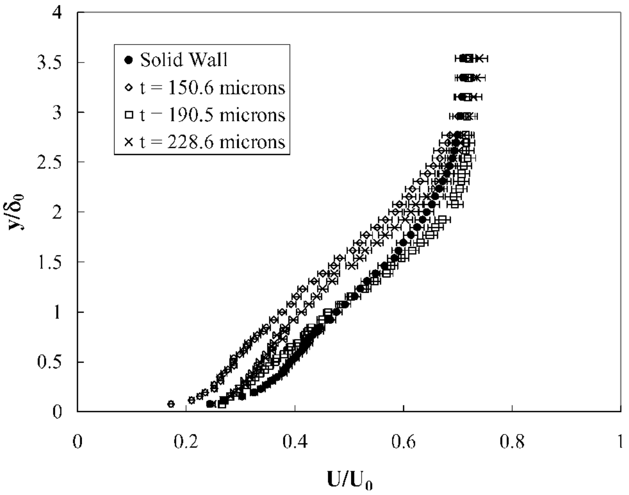

b) Four-flap MART arrays

Fig. 8 Outgoing velocity profiles ($x^* = 23.0$).

Figure 8a depicts the outgoing boundary-layer profiles of three six-flap MART arrays at the furthest downstream location, $x^* = 23.0$. The solid-wall reference case is also presented for comparison purposes. As a result of the SBLI, the outgoing velocity profiles for all cases are not nearly as full as the incoming boundary layer (Fig. 7), as expected. Furthermore, the boundary layer is seen to thicken by a factor of approximately three through the interaction, consistent with the shadowgraph visualizations.

The velocity profiles of the six-flap 63.5- and 150.6-μm MART arrays studied are nearly identical and are clearly not as full as the solid-wall reference case. The profile of the 101.9-μm MART array is significantly fuller than for the other two MART cases, and it approaches, but is not quite as full as, the solid-wall reference case. These observations, coupled with the static pressure distributions of Fig. 6a, suggest that the optimum thickness of the six-flap MART arrays is near 101.9 μm. For the 63.5-μm thickness, the flap deflections are apparently too large, causing excess recirculation and injection/bleed of the boundary layer. At 150.6 μm, the flap deflections appear to be too small, causing the system to revert to a conventional recirculating control device, with transverse injection and bleed. This supports the principle on which the flap designs are based: Tangentially oriented injection and bleed will lead to improved boundary-layer characteristics.

Figure 8b depicts velocity profiles for the four-flap MART arrays at the same streamwise location, $x^* = 23.0$. With the four-flap arrays, flap thickness has a more demonstrable effect on the velocity profiles than with the six-flap arrays of Fig. 8a. The velocity profiles in Fig. 8b indicate a trend identical to the six-flap velocity profiles, suggesting that the middle thickness, 190.5-μm, is the optimum; indeed, the velocity profile of the 190.5-μm array appears significantly fuller than the solid-wall reference case near the freestream edge. This indicates that the boundary layer is significantly thinner than the reference case, as preliminarily indicated by the shadowgraph visualizations.

Although total pressure P_t distributions were not measured directly to avoid probe interference effects, they were estimated herein using the nonintrusive measurements. Combining the LDV velocity profiles with the measured stagnation temperature, Mach number profiles were constructed, under the assumption of adiabatic flow conditions. The local static-to-total pressure ratio P/P_t was then computed using the isentropic relation. If the downstream streamlines are approximately straight and there is no interaction with a shock wave or expansion fan, it can be reasonably assumed that static pressure is constant across the boundary layer. The appropriateness of this assumption for certain flow regions can be determined by careful examination of the associated shadowgraphs. Thus, total pressure profiles were estimated for certain regions using the local P/P_t ratio and the measured wall-static pressure (Fig. 6).

The conditions at $x^* = 12.0$ and 15.7 did not allow for the constant static pressure assumption, due to the interaction of the secondary shock with the boundary layer near these streamwise locations (Fig. 4); however, at $x^* = 19.3$ and 23.0, there are no interactions with shock waves or expansion fans, and the streamlines can be assumed to be relatively straight. This allows for the assumption of constant static pressure across the boundary layer, and the subsequent calculation of the total pressure profiles illustrated in Fig. 9.

The total pressure profiles of the six-flap MART arrays are presented in Fig. 9a. Again, the 63.5- and 150.6-μm flaps perform almost identically, and the 101.9-μm flaps show the highest total pressure recovery. None of the arrays, however, demonstrate improved total pressure recovery when compared to the solid-wall reference case. This is consistent with the reduction in static pressure recovery evident in Fig. 6a and the mean velocity profiles presented in Fig. 8a.

The total pressure profiles of the four-flap arrays in Fig. 9b contrast significantly with those of the six-flap arrays. The difference between flap cases is much more pronounced, which is consistent with the more pronounced differences in static pressure and mean velocity profiles (Figs. 6b and 8b). Furthermore, the total pressure profile of the 190.5-μm flaps shows significant improvement over the solid wall. This provides quantitative evidence that this array does, indeed, provide a lambda-shock benefit, as qualitatively suggested by the shadowgraph visualizations. Although other recirculating control studies have demonstrated this benefit, the increase in total pressure recovery demonstrated by the 190.5-μm flaps is significantly greater than that found in previous studies.[5,6,10,12]

An equally significant result of this study is the effect of the MART system on boundary-layer integral properties. Although the velocity profiles of Fig. 8 give preliminary evidence of the behavior of these parameters, Figs. 10 and 11 give a deeper insight into the effect of the mesoflap arrays on boundary-layer characteristics.

Figure 10a shows the streamwise incompressible displacement thickness evolution of the six-flap MART arrays, again with the solid wall as a reference. In all cases, displacement thickness slightly

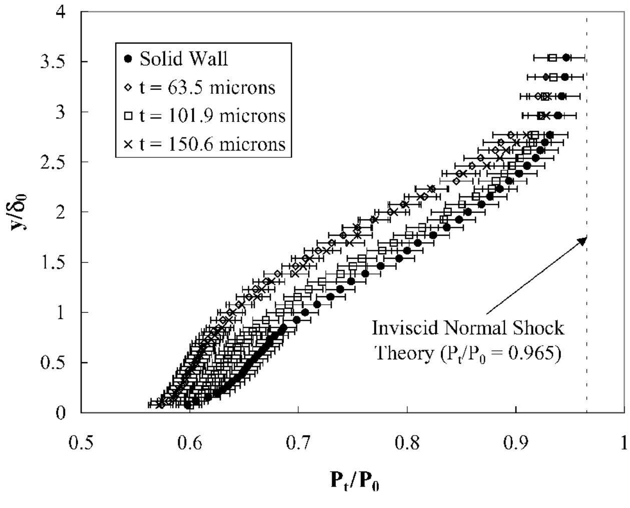

a) Six-flap MART arrays

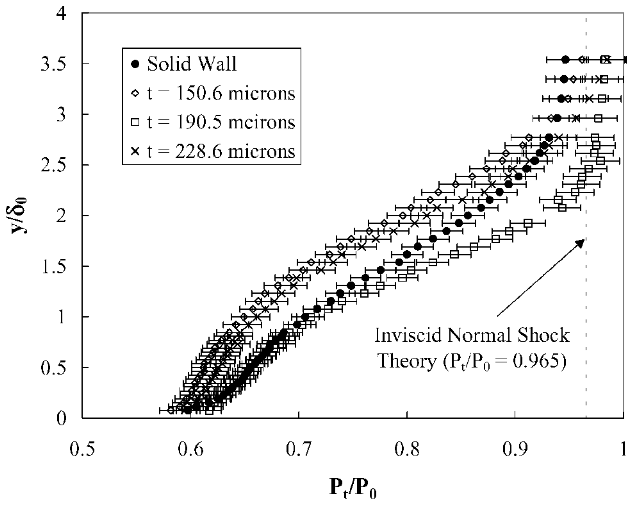

b) Four-flap MART arrays

Fig. 9 Total pressure profiles ($x^* = 23.0$).

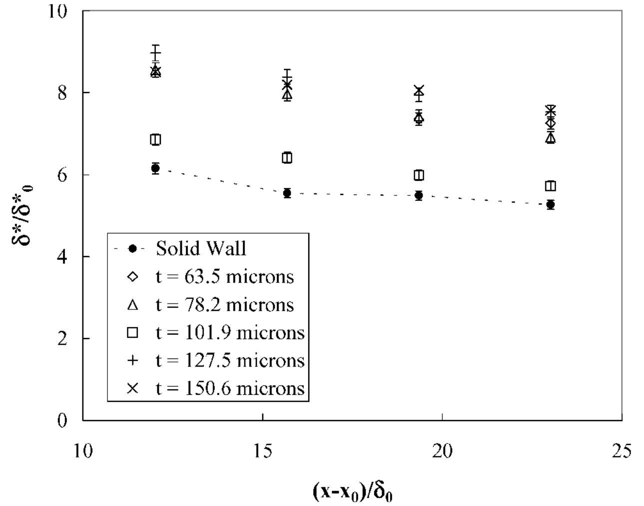

a) Six-flap MART arrays

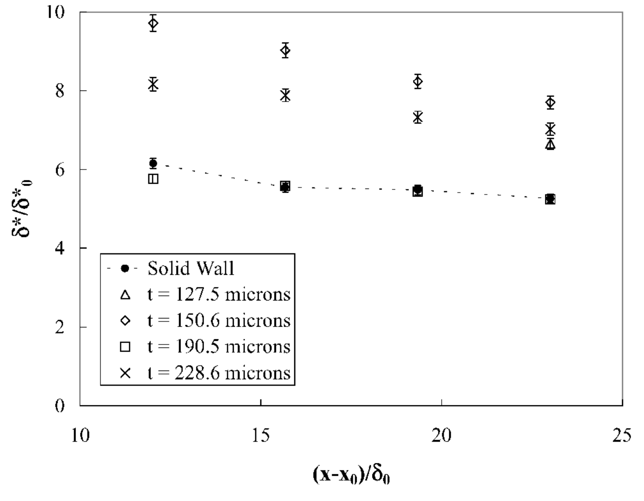

b) Four-flap MART arrays

Fig. 10 Displacement thickness evolution.

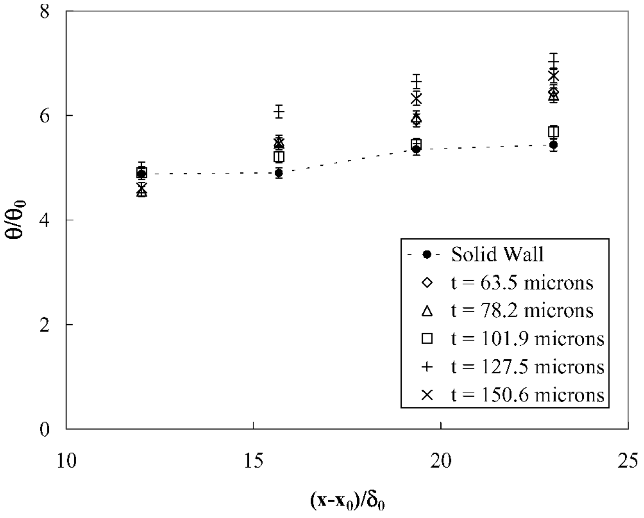

a) Six-flap MART arrays

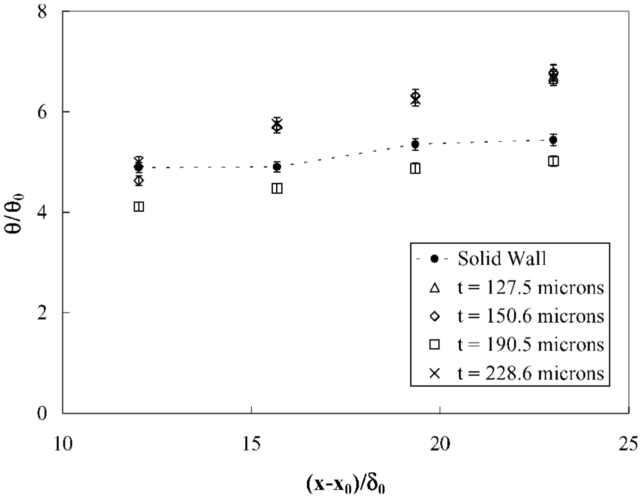

b) Four-flap MART arrays

Fig. 11 Momentum thickness evolution.

decreases with increasing streamwise distance downstream of the SBLI. This behavior is characteristic of a recovering boundary layer. The 63.5-, 78.2-, 127.5-, and 150.6-μm flaps have very similar displacement thicknesses at all four stations; however, the thinner flaps (63.5 and 78.2 μm) do have a slightly smaller displacement thickness than the thicker flaps (127.5 and 150.6 μm). It is clear, though, that the 101.9-μm flap array has the smallest displacement thickness at all four stations. In fact, the displacement thickness of the 101.9-μm flap array is about 20% lower than the other four six-flap MART arrays. The displacement thickness of the 101.9-μm flaps, is, however, consistently higher than for the solid wall by about 10%.

The displacement thickness evolution of the four-flap MART arrays (Fig. 10b) yields more encouraging results. Although the displacement thickness for the 150.6-μm MART array is much larger than for the solid wall, the 190.5-μm MART array has a displacement thickness evolution nearly identical to the solid wall. Indeed, at the last three stations, the square markers that denote the 190.5-μm MART array are essentially covered by the filled circles that denote the solid wall, with a slightly smaller displacement thickness at the first station. The displacement thickness evolution of the 127.5-μm array was captured only at the fourth station and, interestingly, lies midway between that of the 150.6- and 190.5-μm arrays. The thickest four-flap array tested (228.6 μm) possesses a displacement thickness significantly larger than the reference case, but is markedly lower than that of the 150.6-μm array.

The evolution of incompressible momentum thickness of the six-flap MART arrays can be found in Fig. 11a. In all cases, momentum thickness increases slightly with increasing streamwise distance. The momentum thickness evolution of the six-flap MART arrays is qualitatively similar to the displacement thickness evolution: the 127.5- and 150.6-μm MART arrays generally have the largest momentum thickness, followed by the 63.5- and 78.2-μm MART arrays. Again, the momentum thickness for the 101.9-μm MART array approaches that for the solid wall, but is slightly larger. Interestingly, this trend is violated at the first station ($x^* = 12.0$), where the momentum thicknesses of all cases examined are tightly bunched together, with a slight reduction in momentum thickness evident for the 78.2- and 150.6-μm arrays. Another point of interest is the slope of the momentum thickness axial evolution. Specifically, the rate of increase in momentum thickness is greater for the 63.5-, 78.2-, 127.5-, and 150.6-μm MART arrays, compared to both the solid wall and the 101.9-μm MART array. This is in contrast to the displacement thickness evolution depicted in Fig. 10a, where the downward slope of all cases is much more similar.

Figure 11b depicts the momentum thickness evolution of the four-flap MART arrays. The momentum thickness of the 150.6-μm array starts out slightly lower than for the solid wall at station 1 ($x^* = 12.0$), but quickly increases to a value approximately 20% greater than for the solid wall. The 228.6-μm array has a nearly identical momentum thickness evolution, with a slightly larger momentum thickness at station 1. The 190.5-μm MART array, however, has a significantly smaller momentum thickness at all four stations than for the solid wall, by about 10%.

These findings support a significant attribute of the four-flap 190.5-μm MART array: the flaps not only perform the best in terms of total pressure recovery, but also possess the best outgoing boundary-layer characteristics in terms of reduced integral thicknesses. This finding is especially compelling when compared to previous recirculating control studies, for which the increase in total pressure recovery is invariably compromised by a significant increase in boundary-layer integral thicknesses, which typically leads to increased viscous drag.[6] However, this result also demonstrates the sensitivity of flow-control performance to flap design.

Summary

Experiments were conducted on a series of mesoflap arrays in an effort to investigate the potential of the flaps to control normal SBLIs with primary emphasis on supersonic inlet applications. It was found that the thickness of the MART arrays and, therefore, the deflection and transpiration rate, had a demonstrable effect on both pressure recovery and boundary-layer integral properties. Furthermore, varying the thickness of the four-flap arrays had a much larger impact on performance results than variations of six-flap array thickness. Although some of the arrays did not provide a benefit, one particular MART array, the four-flap 190.5-μm thick array, was found to have a significant increase in total pressure recovery over the solid-wall reference case. Furthermore, the boundary-layer integral parameters for this array were seen to improve, with a 10% reduction in momentum thickness while maintaining an unchanged displacement thickness. These improvements demonstrate the potential of the MART system to impact SBLIs positively, which can be important for supersonic inlet design where total pressure recovery and flow uniformity are of prime importance.

Acknowledgments

This work was supported under Contract F49620-98-1-0490 by the Defense Advanced Research Projects Agency with R. W. Wlezien as Technical Monitor and the U.S. Air Force Office of Scientific Research with S. H. Walker as Technical Monitor. The authors also gratefully acknowledge the technical assistance and direction of S. T. McIlwain and D. O. Davis.

References

[1] Gridley, M. C., and Walker, S. H., "Advanced Aero-Engine Concepts and Controls," AGARD CP-572, 1996.

[2] Bahi, L., Ross, J. M., and Nagamatsu, H. T., "Passive Shock-Wave/Boundary-Layer Control for Transonic Airfoil Drag Reduction," AIAA Paper 83-0137, Jan. 1983.

[3] Raghunathan, S., and Mabey, D. G., "Passive Shock-Wave/Boundary-Layer Control on a Wall-Mounted Model," *AIAA Journal*, Vol. 25, No. 2, 1987, pp. 275–278.

[4] Raghunathan, S., "Passive Control of Shock-Boundary Layer Interaction," *Progress in Aerospace Sciences*, Vol. 25, No. 3, 1988, pp. 271–296.

[5] Raghunathan, S., and McIlwain, S. T., "Further Investigations of Transonic Shock Wave/Boundary-Layer Interaction with Passive Control," *Journal of Aircraft*, Vol. 27, No. 1, 1990, pp. 60–65.

[6] Bur, R., Corbel, B., and Delery, J., "Study of Passive Control in a Transonic Shock Wave/Boundary-Layer Interaction," *AIAA Journal*, Vol. 36, No. 3, 1998, pp. 394–400.

[7] Bur, R., Benay, R., Corbel, B., and Delery, J., "Physical Study of Shock Wave/Boundary-Layer Interaction Control in Transonic Flow," AIAA Paper 2000-0933, Jan. 2000.

[8] McCormick, D. C., "Shock/Boundary-Layer Interaction Control with Vortex Generators and Passive Cavity," *AIAA Journal*, Vol. 31, No. 1, 1993, pp. 91–96.

[9] Lin, Y. L., Rimlinger, M. J., Shih, T. I., and Willis, B. P., "Control of Shock Wave/Boundary-Layer Interactions with Passive Blowing and Bleeding," AIAA Paper 97-3002, July 1997.

[10] Gefroh, D. L., Hafenrichter, E. S., Ford, B. M., Dutton, J. C., McIlwain, S. T., and Loth, E., "Experimental Study of Mesoflaps for SBLI Control," AIAA Paper 2000-0355, Jan. 2000.

[11] Wood, B., Loth, E., Geubelle, P., and McIlwain, S. T., "A Numerical Methodology for an Aeroelastic SBLI Flow," AIAA Paper 2000-0552, Jan. 2000.

[12] Gefroh, D. L., Hafenrichter, E. S., McIlwain, S. T., Loth, E., Dutton, J. C., and Geubelle, P. H., "Simulation and Experimental Analysis of a Novel SBLI Flow Control System," AIAA Paper 2000-2237, June 2000.

[13] Gefroh, D. L., "Experimental Study of Mesoflaps to Control Oblique Shock/Boundary-Layer Interaction," M.S. Thesis, Dept. of Aeronautical and Astronautical Engineering, Univ. of Illinois at Urbana–Champaign, Urbana, IL, May 2000.

[14] Amatucci, V. A., Dutton, J. C., Kuntz, D. W., and Addy, A. L., "Two-Stream Supersonic, Wake Flowfield Behind a Thick Base, Part 1: General Features," *AIAA Journal*, Vol. 30, No. 1, 1992, pp. 43–48.

[15] Carroll, B. F., Dutton, J. C., and Addy, A. L., "NOZCS2: A Computer Program for the Design of Continuous Slope Supersonic Nozzles," Rept. UILU ENG 86-4007, Dept. of Mechanical and Industrial Engineering, Univ. of Illinois at Urbana–Champaign, Urbana, IL, Aug. 1986.

[16] Hafenrichter, E. S., "Experiments on Normal Shock/Boundary Layer Interaction Control Using Aeroelastic Mesoflaps," M.S. Thesis, Dept. of Mechanical and Industrial Engineering, Univ. of Illinois at Urbana–Champaign, Urbana, IL, April 2001.

[17] Carroll, B. F., and Dutton, J. C., "Characteristics of Multiple Shock Wave/Turbulent Boundary-Layer Interactions in Rectangular Ducts," *Journal of Propulsion and Power*, Vol. 6, No. 2, 1990, pp. 186–193.

[18] Santiago, J. G., and Dutton, J. C., "Velocity Measurements of a Jet Injected into a Supersonic Crossflow," *Journal of Propulsion and Power*, Vol. 13, No. 2, 1997, pp. 264–273.

[19] Bloomberg, J. E., "An Investigation of Particle Dynamics Effects Related to LDV Measurements in Compressible Flows," M.S. Thesis, Dept. of Mechanical and Industrial Engineering, Univ. of Illinois at Urbana–Champaign, Urbana, IL, May 1989.

[20] Herrin, J. L., and Dutton, J. C., "An Investigation of LDV Velocity Bias Correction Techniques for High-Speed Separated Flows," *Experiments in Fluids*, Vol. 14, Nos. 4/5, 1993, pp. 354–363.